

The mini-neutron monitor: A new approach in neutron monitor design

Du Toit Strauss^{1*}, Stepan Poluianov^{2,3}, Cobus van der Merwe¹, Hendrik Krüger¹, Corrie Diedericks¹, Helena Krüger¹, Ilya Usoskin^{2,3}, Bernd Heber⁴, Rendani Nndanganeni⁵, Juanjo Blanco-Ávalos⁶, Ignacio García-Tejedor⁶, Konstantin Herbst⁴, Rogelio Caballero-Lopez⁷, Katlego Moloto¹, Alejandro Lara⁷, Michael Walter⁸, Nigussie Mezgebe Giday⁹ and Rita Traversi¹⁰

¹ Center for Space Research, North-West University, Potchefstroom, South Africa e-mail: dutoit.strauss@nwu.ac.za

² Space Physics and Astronomy Research Unit, University of Oulu, Finland

³ Sodankylä Geophysical Observatory, University of Oulu, Finland

⁴ Institut für Experimentelle und Angewandte Physik, Universität Kiel, Kiel, Germany

⁵ South African National Space Agency, Hermanus, South Africa

⁶ Universidad de Alcalá (UAH), Dpto. Física y Matemáticas and Dpto. Automática, Campus Científico-Tecnológico (Externo), Alcalá de Henares, Madrid, Spain

⁷ Instituto de Geofísica, Universidad Nacional Autónoma de México, México D.F., México

⁸ Deutsches Elektronen-Synchrotron DESY in Zeuthen, Germany

⁹ Department of Space Science and Applications Research, Ethiopian Space Science and Technology Institute, Addis Ababa, Ethiopia

¹⁰ Department of Chemistry “Ugo Schiff”, University of Florence, Italy

ABSTRACT

The near-Earth cosmic ray flux has been monitored for more than 70 years by a network of ground-based neutron monitors (NMs). With the ever-increasing importance of quantifying the radiation risk and effects of cosmic rays for, e.g., air and space-travel, it is essential to continue operating the existing NM stations, while expanding this crucial network. In this paper, we discuss a smaller and cost-effective version of the traditional NM, the mini-NM. These monitors can be deployed with ease, even to extremely remote locations, where they operate in a semi-autonomous fashion. We believe that the mini-NM, therefore, offers the opportunity to increase the sensitivity and expand the coverage of the existing NM network, making this network more suitable to near-real-time monitoring for space weather applications. In this paper, we present the technical details of the mini-NM’s design and operation, and present a summary of the initial tests and science results.

Key words. neutron monitors – space weather instrumentation – cosmic rays – neutron monitor multiplicity

1. Introduction

Cosmic rays, including sporadic solar energetic particle (SEP) events, are the dominant source of hazardous atmospheric radiation at, and above, aviation altitudes, making the long-term monitoring of cosmic ray levels essential. The latter is especially important since the International Civil Aviation Organization’s (ICAO’s)¹ recent amendments to the meteorological procedures to include space weather warnings and/or predictions as part of flight planning. A reliable near real-time estimate of the cosmic ray flux is therefore essential. Moreover, ICAO requires ground-based cosmic ray observations that can serve as a proxy for the levels of radiation at aviation altitudes, making the *neutron monitor* (NM) a reference space weather instrument for aviation

dosimetry studies, but also more generally for monitoring the levels of cosmic radiation that may cause unwanted effects, including single-event upsets (see e.g. [Taber and Normand, 1993](#); [Dyer et al., 2007, 2009](#)), in avionics and other sensitive electronics devices (see also the IEC 62396-1:2016 standard²).

For more than 70 years, NMs have been the most cost-effective instrument to monitor the levels of cosmic radiation near Earth (see the recent review by [Bütikofer, 2018](#)). These instruments, however, do not measure the cosmic radiation directly, but rather the flux of secondary and tertiary neutrons produced in the atmosphere, and in the detector itself. The count rate of an NM can thus be written, in the most basic formulation, as

$$N(P_c, t) = \sum_i \int_{P_c}^{\infty} j_i(P, t) Y_i(P, t, \dots) dP, \quad (1)$$

* Corresponding author: e-mail: dutoit.strauss@nwu.ac.za

¹ ICAO State Letter, Proposals for the amendment of Annex 3 and consequential Amendments to Annex 15, PANSABC and PANSATM, AN 10/117/41, 7 April 2017.

² Available at <https://webstore.iec.ch/publication/24053>.

where P_c is the cutoff rigidity (minimum rigidity particle that can reach the detector), i represents the particle distribution under consideration (e.g. protons and heavier nuclei), and $Y_i(P, t, \dots)$ is the so-called yield function that represents the response of the instrument on the unit flux of primary cosmic rays with rigidity P , including atmospheric and instrumental effects. The latter therefore depends on various parameters that are unique to each monitor (see e.g. Caballero-Lopez, 2016; Clem and Dorman, 2000). In order to reconstruct the primary cosmic ray flux, $j_i(P, t)$, the yield function must be known for a number of stations characterized by different P_c values (e.g. Mishev et al., 2020). Once the atmospheric yield functions are known, continuous spectral information about cosmic ray modulation (primary spectra above the atmosphere and magnetosphere) can be obtained from neutron monitor differential response functions. These response functions can be derived from the count rates of the world-wide neutron monitor network if individual NMs are inter-calibrated (e.g. Moraal et al., 2001).

To inter-calibrate the world-wide network of NMs, Moraal et al. (2001) initiated the development of a smaller and lighter version of the standard neutron monitor, a *calibration NM*. The aim was to design a portable NM that can easily be shipped and installed, even at very remote locations. Although this calibration process was mostly successful (e.g. Krüger et al., 2003), it was quickly realized that, under the right circumstances, a calibration NM's data can be of sufficient quality to supplement the measurements of traditional NMs. It was subsequently proposed by Krüger et al. (2015) to refer to these smaller monitors as *mini-NMs*, with mini-NMs installed at the Concordia (Poluianov et al., 2015; Usoskin et al., 2015) and Neumayer III (Heber et al., 2015) research stations in Antarctica. Since then, the mini-NM's design has been constantly optimized and the counting electronics updated. In this paper, we describe the most recent version of the mini-NM, including mechanical design, electronics systems, and software implemented, along with initial tests of the data acquired.

2. Basic neutron monitor design

The design of the basic NM has changed very little over the years since its first development (see the review by Simpson, 2000), until the most recent implementation (e.g. Signoretto and Storini, 2011; Medina et al., 2013; Jung et al., 2016), consisting of an outer reflector (shielding the instrument from external thermal neutrons, while containing neutrons produced within the NM), a lead producer (producing additional low energy neutrons via nuclear interactions to increase the monitor's detection efficiency), and an inner moderator (thermalizing the newly produced neutrons). The thermal neutrons are then counted via pulses produced in a proportional counter tube, traditionally filled with either BF_3 or ^3He gas. For both of these filling gases, an electrical pulse is produced via a neutron capture process (Knoll, 2010), i.e.

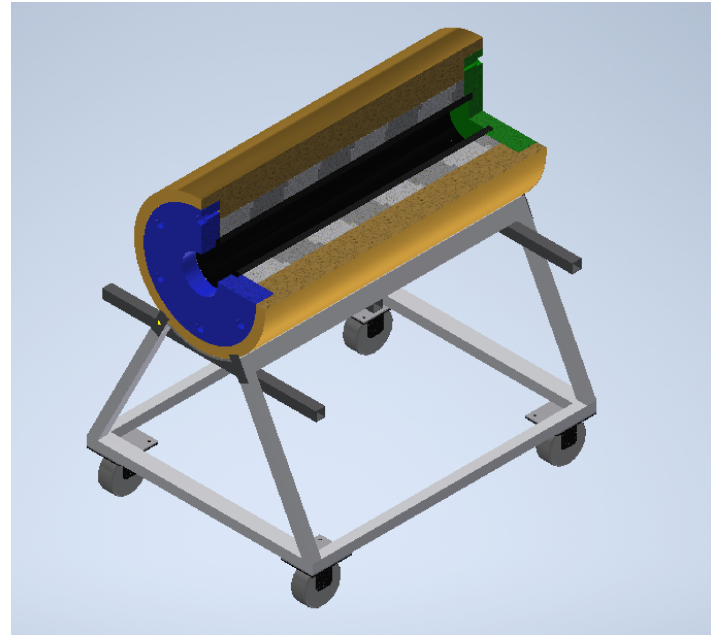
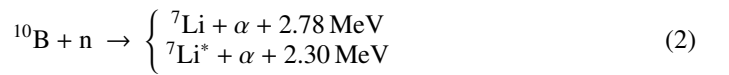
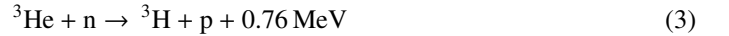


Fig. 1: A sketch of the standard mini-NM set-up. The reflector (yellow), moderator (black), front- and end-cap (blue and green), and lead rings (dark and light gray) are indicated.



or



that ionizes a small portion of the filling gas. Note that only a small fraction ($\sim 6\%$) of the reactions leaves ^7Li in the ground state, releasing 2.78 MeV in kinetic energy, while the majority of the reactions leave ^7Li in the first excited state, releasing only 2.3 MeV in kinetic energy. Some NMs, sometimes referred to as *neutron moderated detectors* (NMDs), do not have the lead producer and are sensitive to neutrons in a slightly lower energy range. These NMDs are referred to as “bare”, lead-free detectors, or even “wax” NMs in certain texts where the reflector and moderator in older set-ups were manufactured from paraffin wax. The physics of neutron detection in NMs and NMDs are identical, but the count rates of NMDs are usually lower, and the instrument responds to lower energy incident particles, due to the absence of a producer.

2.1. Mechanical design

A sketch of the standard mini-NM design is shown in Figure 1. The outer reflector consists of the main cylinder (yellow) and front and end covers (blue and green), manufactured from 75mm thick rolled polyethylene sheets. Lead rings of a maximum diameter of 206mm are shown in light and dark gray, while the inner

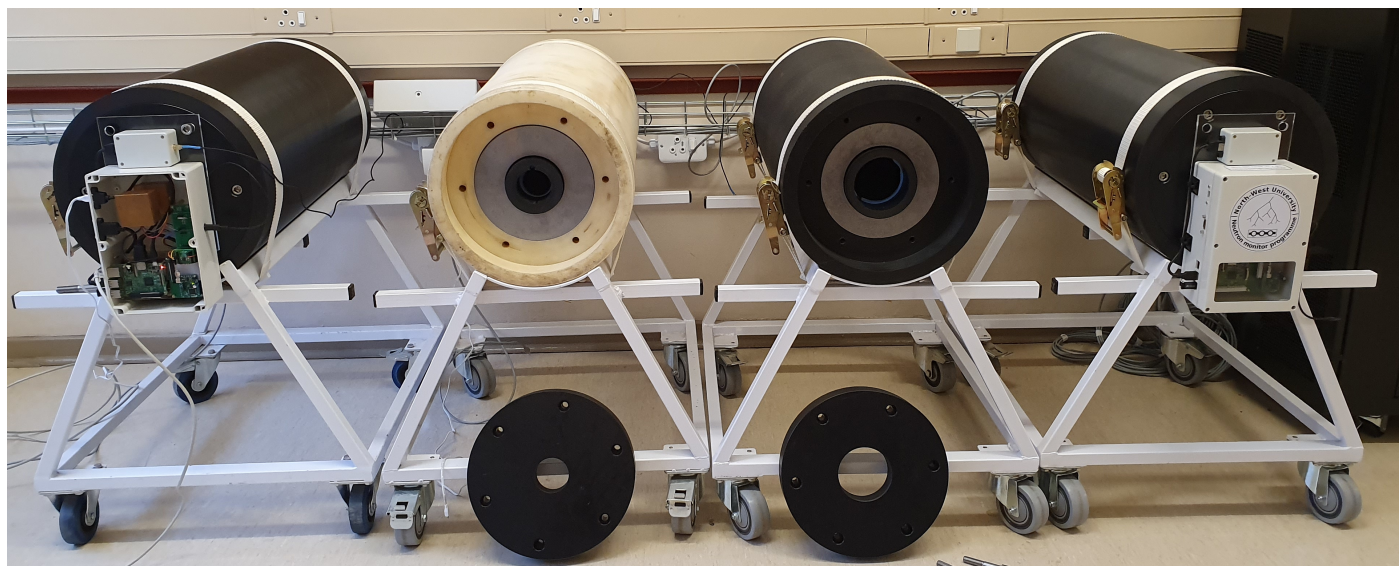


Fig. 2: Mini-NMs undergoing testing. The front covers were removed on two monitors to show the lead rings and the internal moderators.

moderator (black) is also manufactured from rolled polyethylene sheets of thickness 15mm. The inner diameter of the lead rings, and the diameter of the moderator, is determined by the type of tube used in the monitor. For the purpose of this study, we have used three different tubes, with details summarized in Table 1. The completed mini-NM set-up, while undergoing testing, is shown in Figure 2. The dimensions of a completed mini-NM, with a trolley stands, are approximately 900mm (height) \times 700mm (width) \times 800mm (length) and the weight is approximately 250/100 kg with/without the lead rings.

The volume of a mini-NM detector is notably smaller than that of a full-size standard NM64 (the 64 referring to the standardized NM set-up implemented in 1964 during the International Quiet Sun Year; IQSY). However, with a change in regulations of the ICAO, related to the transport of dangerous goods³, it became possible to significantly increase the allowed maximal pressure of the BF₃ tubes. The pressure in a mini-NM detector LND2043 is 930 mbar, while it is only 300 mbar in a standard NM64 detector. This partly compensates for the reduced efficiency of the mini-NM as compared to the much larger full-size NM64.

2.2. Electronics

Although the mechanical design of a mini-NM, similar to a standard NM, is simple, the associated electronics are usually the most complicated part. In designing the new version of the mini-NM's electronics, it was decided to use, as much as possible, affordable, off-the-shelf components. In addition, it was decided to design the electronics in a modular fashion, where defective parts

³ <https://www.icao.int/safety/DangerousGoods/Pages/DGP23-Report.aspx>

can be quickly (and cheaply) replaced. A sketch of the electronics head is shown in the left panel of Figure 3, while the right panel shows a finished unit. The different components are briefly discussed below.

2.2.1. Raspberry Pi micro-computer

A Raspberry Pi 3 B⁴, a fully-functional single-board computer with GNU/Linux operating system is used to interface with the system components. Not only does the Raspberry Pi offer a significant amount of computing power but it also simplifies a number of data processing tasks: The on-board computing power enables data processing and data validation in real-time. This allows functionality like digital filters and enables units to alert or automatically reset if an error occurs. The built-in network interface allows for remote monitoring, administration, and data synchronisation. The USB (universal serial bus) interface allows for a local data backup when network connectivity is interrupted or unavailable. The weakness of the Raspberry Pi is the limited write cycles on the SD (secure digital) card. This can be overcome by using Linux shared memory for intermediate data recording and higher quality (e.g. industrial rated) SD cards.

2.2.2. High voltage supply

The high voltage supply consists of a microprocessor and a set of voltage doubler circuits also known as a Cockroft-Walton multiplier. A PID (proportional integral derivative) controller adjusts a pulse width modulated input signal to regulate the output voltage. The desired voltage is sent to the microcontroller over a serial connection, and the voltage value is returned to the Raspberry Pi. The output range of the high voltage supply can

⁴ <https://www.raspberrypi.org/>

Table 1: Comparison of the different tubes used for testing^a.

| Tube naming | Gas | Outer diameter (mm) | Length (mm) | Recommended voltage (V) |
|-------------|----------|---------------------|-------------|-------------------------|
| BF3 | LND2043 | BF ₃ | 89 | 2120 – 2370 |
| BF3(thin) | LND20366 | BF ₃ | 51 | 900 – 1150 |
| He3 | LND25373 | ³ He | 51 | 1200 – 1450 |

^a Tubes are manufactured by LND Inc., USA and available through <https://www.lndinc.com/>.

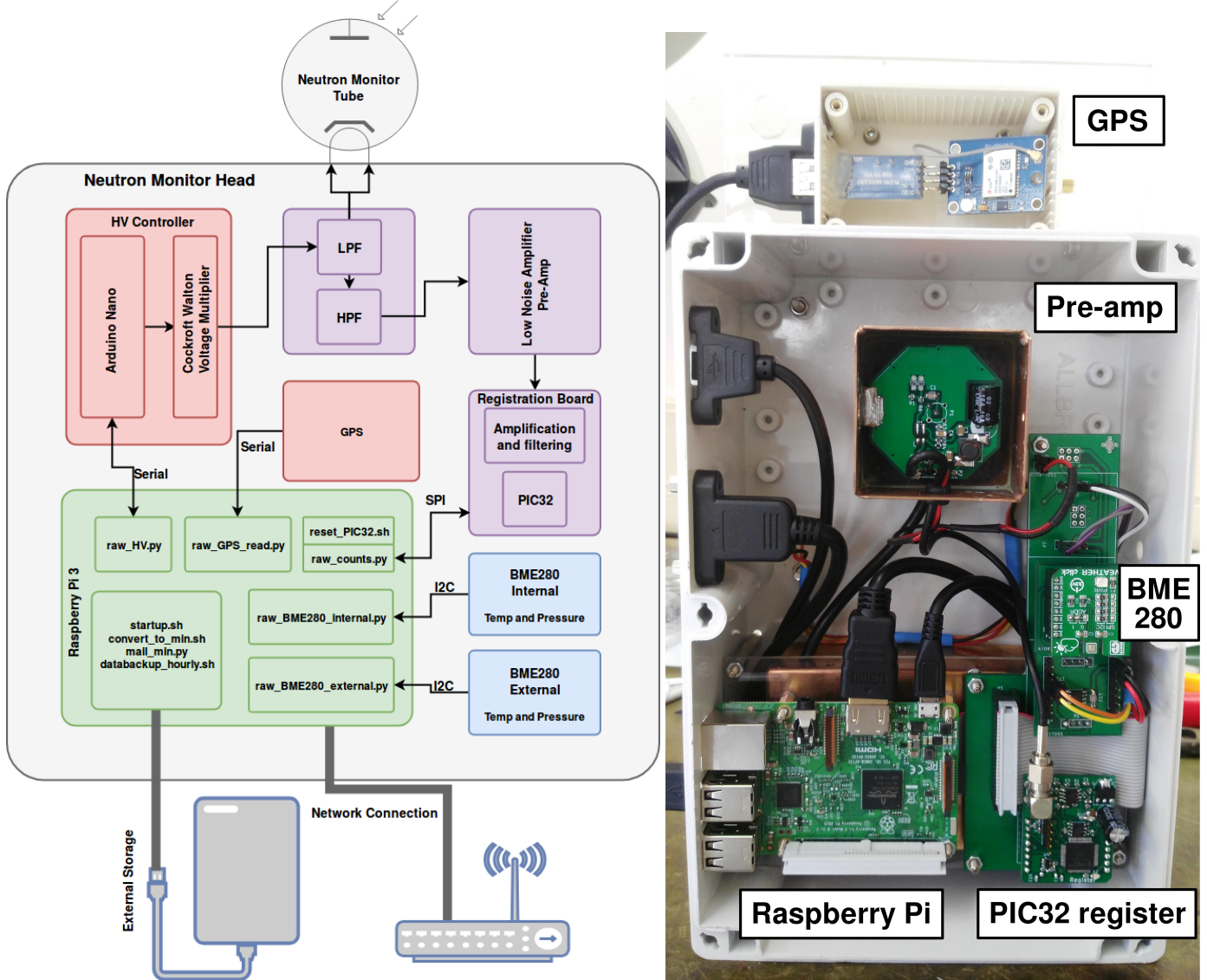


Fig. 3: The left panel shows a schematic representation of the mini-NM electronics head while the right panel shows the actual components, with the front cover removed.

be set between 0.8 – 4 kV, where the maximum voltage is also dependent on the inductance of the transformer, which can also be adjusted. The 5 V signal from the microcontroller switches a transistor which supplies a flyback transformer before the multiplication stage. This high-voltage power supply design is

feasible as the neutron monitor tube requires very little current. The only real concern is the long term voltage stability and minimal high-frequency noise, which is less than 1 mV on 4 kV.

2.2.3. Pre-amplifier

The pre-amplifier uses a low noise MOSFET (metal-oxide-semiconductor field-effect transistor) for its first amplification stage. A DC (direct current) blocking capacitor is used to filter the pulses from the high voltage on the neutron monitor cathode. The MOSFET's low gate current allows the filtered pulses to trigger the amplifier. Careful design considerations were made with regard to the input impedance and sensitivity of the pre-amplifier. The input impedance determines the shape of the amplified pulse, and over biasing will make the MOSFET too sensitive with the result that amplified noise will then dominate the later stages of the system. The pre-amplifier is a critical component, and variations between heads are most likely related to manufacturing tolerances in the MOSFET and its biasing components. Band-pass filters are used in the second stage of amplification to suppress any noise from the pre-amplifier and to shape the amplified pulses.

2.2.4. Analogue-to-digital converter

A dedicated PIC32 microcontroller is used to sample the incoming pulses, after amplification, with a 10-bit analog-to-digital converter (ADC). The pulses are sampled at 2 MHz and stored in the microcontroller's buffer. The sampling discriminator can be set in software, only triggering samples above the set value. This software filter allows for further elimination of noisy data. The Raspberry Pi software interfaces with the PIC32 via SPI (serial peripheral interface) and clears the sample buffer. The raw pulse data is stored and processed by the Raspberry Pi software.

2.2.5. Peripherals

The environmental conditions are measured with two Adafruit⁵ BME280 sensor boards (the BME sensor itself is produced by Bosch.⁶) The BME280 sensor has a maximum absolute offset of 1 mbar, and a relative error of 0.12 mbar. We have, however, performed long-term tests of this sensor and have found any possible offsets to be constant over time. The relative (noise) error is further decreased in the mini-NM by sampling the pressure every second and using one-minute averages for all calculations. We believe that the BME sensor provides a very affordable and accurate alternative to the more expensive barometers currently used. Data is sent to the Raspberry Pi via an I2C (inter-integrated circuit) connection. Internal (meant to be placed against the tube inside of the moderator) and external (placed inside the electronics enclosure) pressure/temperature sensors are available. A redundant pressure measurement can also help with the identification of any possible absolute calibration issues when installing a new pressure sensor or to test for possible drifts in a defective sensor.

⁵ <https://www.adafruit.com/product/2652>

⁶ <https://www.bosch-sensortec.com/products/environmental-sensors/gas-sensors-bme680/>

The default time synchronization is realized with the Network Time Protocol (NTP), when the mini-NM receives time signals from an NTP server via a network connection. However, there is an optional GPS (global positioning system) unit that can be connected via a USB connector on the Raspberry Pi that sends location data and a signal for time synchronisation (when an NTP server is not available) over the USB-serial connection.

2.3. Software

Similar to the electronics, the software used on the mini-NM was designed to be modular with scripts written using the Python programming language⁷ or simple shell scripts. Specific scripts, therefore, have very specific purposes, e.g., a stand-alone Python script is used to read the raw GPS data over a serial connection and write the raw data to a file located on the Raspberry Pi. Similar scripts read data from the ADC, the BME sensors, and communicate with the Arduino nano⁸ which controls the HV. Once the raw data are collected in their native time resolution, the data is averaged into one-minute time resolution.

These scripts are continually being refined and updated, with the latest version available through a Creative Commons non-commercial license⁹.

3. Testing: Neutron source

Initial testing of the mini-NM was performed with an ²⁴¹Am-⁹Be neutron source to improve measurement statistics, but also to eliminate any possible environmental dependences.

3.1. Pulse height-width diagrams

The left panel of Figure 4 shows a selection of pulses read-out of the mini-NM with the thin BF₃ tube inserted. Based on the maximum pulse height and length (i.e., width) of the pulses, they are divided into counts (indicated by red) and noise (blue curves). The ADC threshold is indicated on this figure as the dashed line at 0.2 V. Once the ADC voltage crosses this threshold, the start of a pulse is registered, and the pulse is digitized until the voltage drops below this level. For each pulse, the amplitude (i.e., maximum pulse height) and length are recorded, and, as discussed in the next section, this is used to discriminate between data and noise.

The right panel of Figure 4 shows a binned 2D histogram of the pulse width and pulse histogram, again for the thin BF₃ tube. The distributions are also projected onto each plane. From the 2D histogram, we can clearly identify low amplitude noise below ~ 0.5 V, consisting of short and longer pulses.

⁷ <https://www.python.org/>

⁸ <https://www.arduino.cc/en/Guide/ArduinoNano>

⁹ https://fskbhel.puk.ac.za/neutronmonitor/Mini_NM/Software_images/

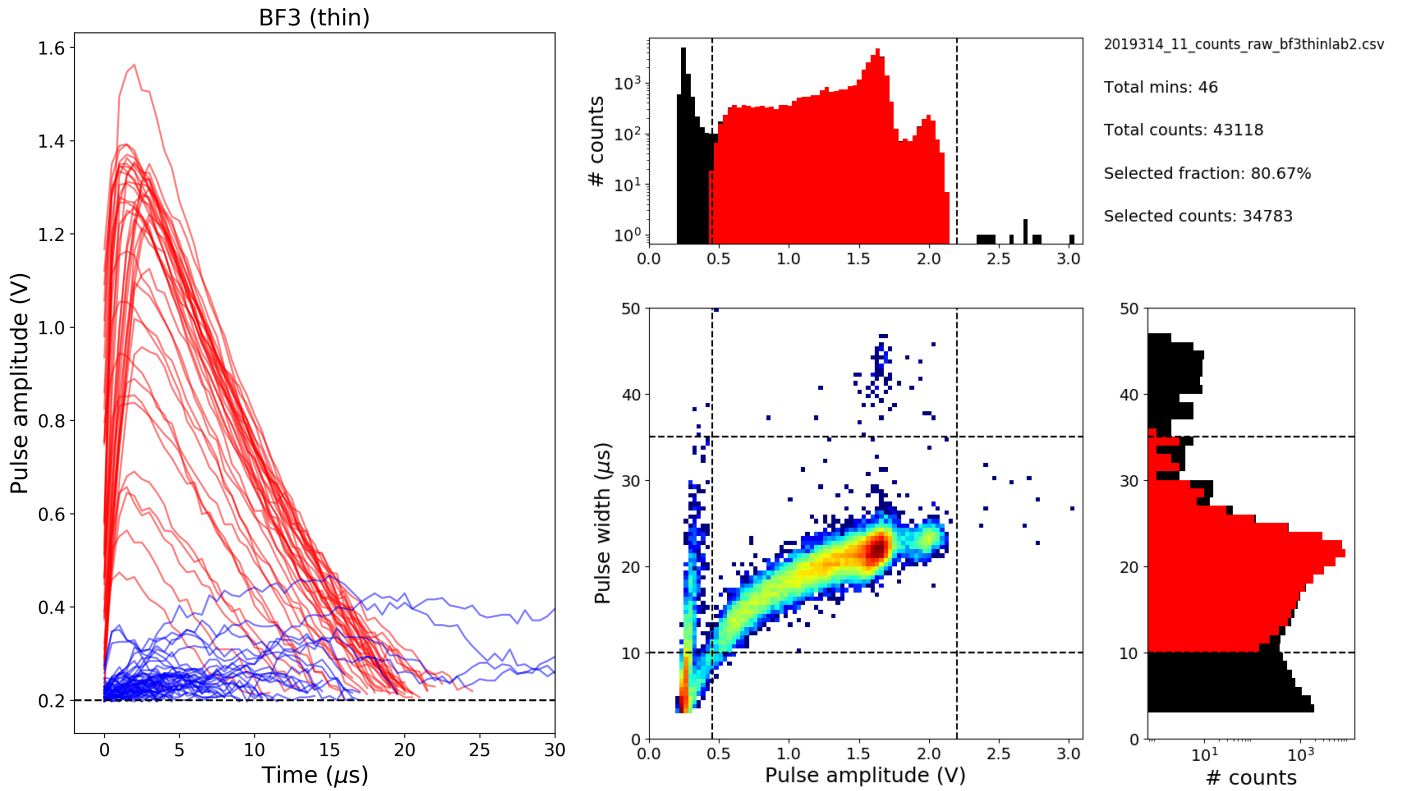


Fig. 4: Left panel: A selection of pulses registered from the thin BF_3 tube. Red pulses are assumed to be observations, while blue pulses indicate noise. Right panel: A 2D pulse width-amplitude histogram as registered from the same tube. The distribution is also projected onto each plane. The dashed lines show the cut applied to the pulses in order to discriminate between measurements and noise. On the projected histograms, all the pulses are indicated by a black histogram, while the red histogram indicated pulses assumed to be measurements free from noise.

Two peaks are observed in the pulse width-amplitude plot, near 1.6 V and 2 V, which is presumably due to the decay into ${}^7\text{Li}^*$ and ${}^7\text{Li}$, respectively. Also note the continuous decreasing pulse amplitude towards lower pulse amplitudes, until the noise threshold is reached. This is, most likely, due to the *wall effect*, resulting in some fraction of energy being deposited into the wall of the detector (see the discussion by e.g. Knoll, 2010).

By calculating and monitoring these distributions on, e.g., an hourly basis, allows us to determine and track the accuracy of the detector: Any external noise (e.g., mechanical vibrations or high-voltage ripple currents) will change the shape of the distributions, allowing us to identify and correct for such events.

Visualizing the pulses in such a 2D plane also allows us to perform a detailed separation of the pulses into noise and/or data (counts) by applying an appropriate cut through the pulse amplitude/width plane. As an example, here we perform a simple square cut (indicated by the dashed lines) and count all the pulses in these regions as data. The projections show all the pulses as black histograms, and selected data as the red histograms. In the future, more complex separation algorithms

can be applied to the pulses.

3.2. Multiplicities

The new hardware design allows us to also examine the waiting time, Δt , between pulses down to the low μs range. For the purpose of this study, we define the waiting time simply as the time between pulses, i.e. the time that elapses from the end of one pulse (ADC drops below the threshold) and the onset of the next (ADC crosses the threshold). The electronics sample at a constant rate of 2MHz, and, in principle, the detector dead-time is only determined by the length of the pulses observed. In a standard NM with the lead producer in place, these so-called *multiplicity* plots show a double-Poisson distribution. Using cosmic ray measurements from the ${}^3\text{He}$ tube, Figure 5 shows a distribution of the waiting time between pulses for a full day of observation of cosmic ray neutrons as the blue histogram in the left panel. The grey and green dashed lines indicate bins with either 1 or 10 counts (data below these lines are considered statistically

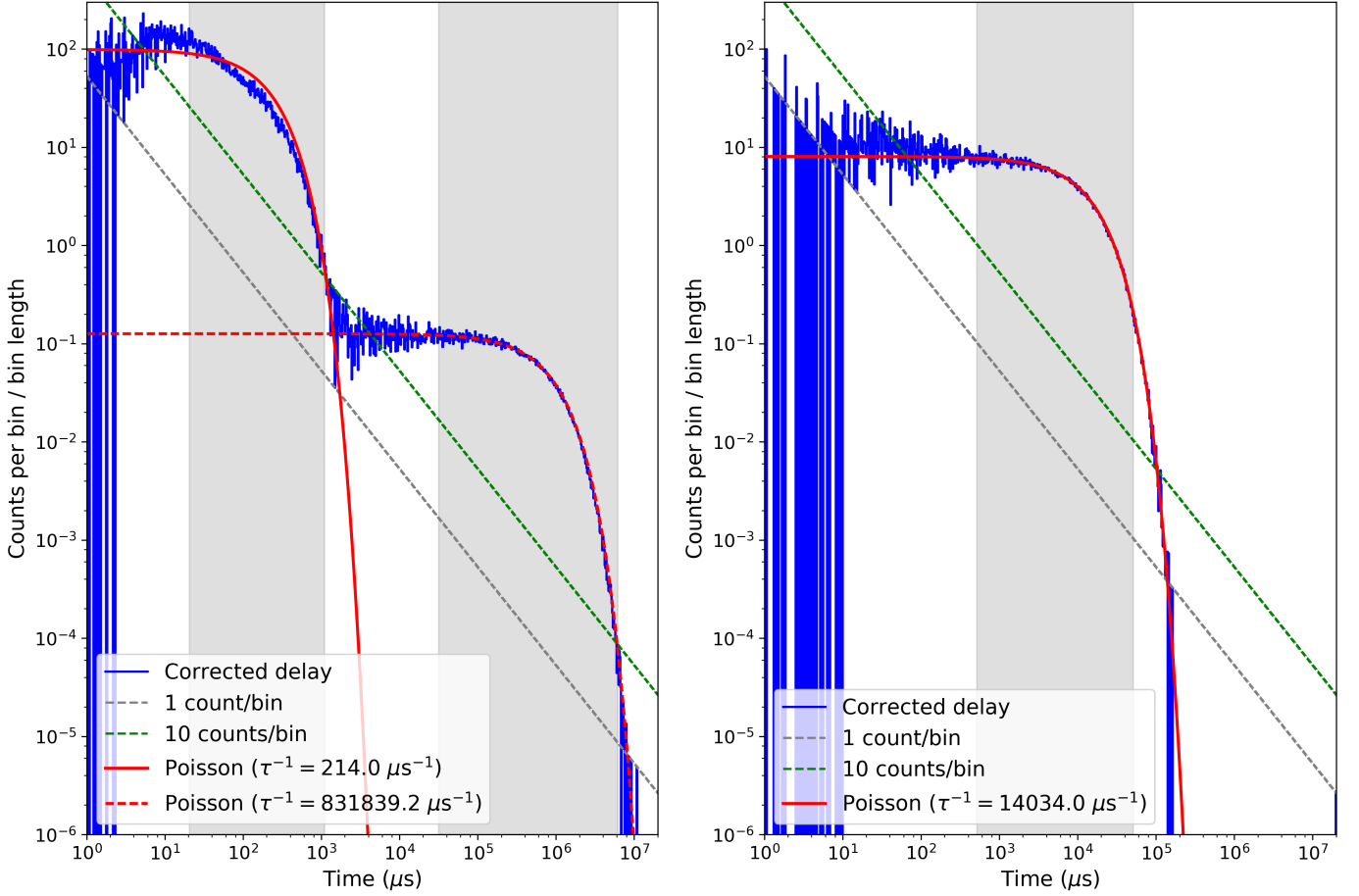


Fig. 5: The waiting time distribution (blue histogram) for cosmic ray neutrons as observed with the ^3He tube (left panel) and for the test source (right panel). The red curves show fitted Poisson distributions, while the dashed gray and green lines indicate bins containing either 1 or 10 counts.

insignificant). The shaded parts of the distribution is used to fit two separate Poisson distributions in the form

$$\mathcal{D}(\Delta t) = \mathcal{D}_0 \exp\left(\frac{\Delta t - \Delta t_0}{\tau}\right), \quad (4)$$

with the resulting values of τ indicated in the legend. The calculated distributions seem consistent with previous observations (e.g. Bieber et al., 2004), where the low Δt distribution is formed by evaporated neutrons produced in the lead producer. These neutrons have a high level of multiplicity, i.e., every incident high-energy proton leads to the formation of a number of neutrons. The high Δt distribution is formed by a combination of low energy neutrons created in the atmosphere, and low-multiplicity neutrons created in the lead producer by low energy protons.

The results for the neutron test source (right panel) shows only a single Poisson distribution, as these low energy neutrons probably interact directly with the ^3He gas, and do not undergo

nuclear reactions with the producer.

3.3. High-voltage plateau

We run the mini-NM tube in the proportionality mode and set the voltage near the observed (and recommended) plateau-region (see, e.g., Kamal, 2014). Although the different tubes' recommended operating voltage regime is given in Table 1, we have also tested the response of each tube's count rate to voltage changes to characterize any possible changes in the count rate due to changing voltages, and to make sure the operating voltages are, in fact, within the HV plateau for each tube. As a default setting, we operate the tubes at the following voltages: BF_3 @ 2300 V, BF_3 (thin) @ 1100 V, and ^3He @ 1350 V. However, with the HV system discussed above, it is easy to adjust this value with simply changing a variable in the corresponding software script.

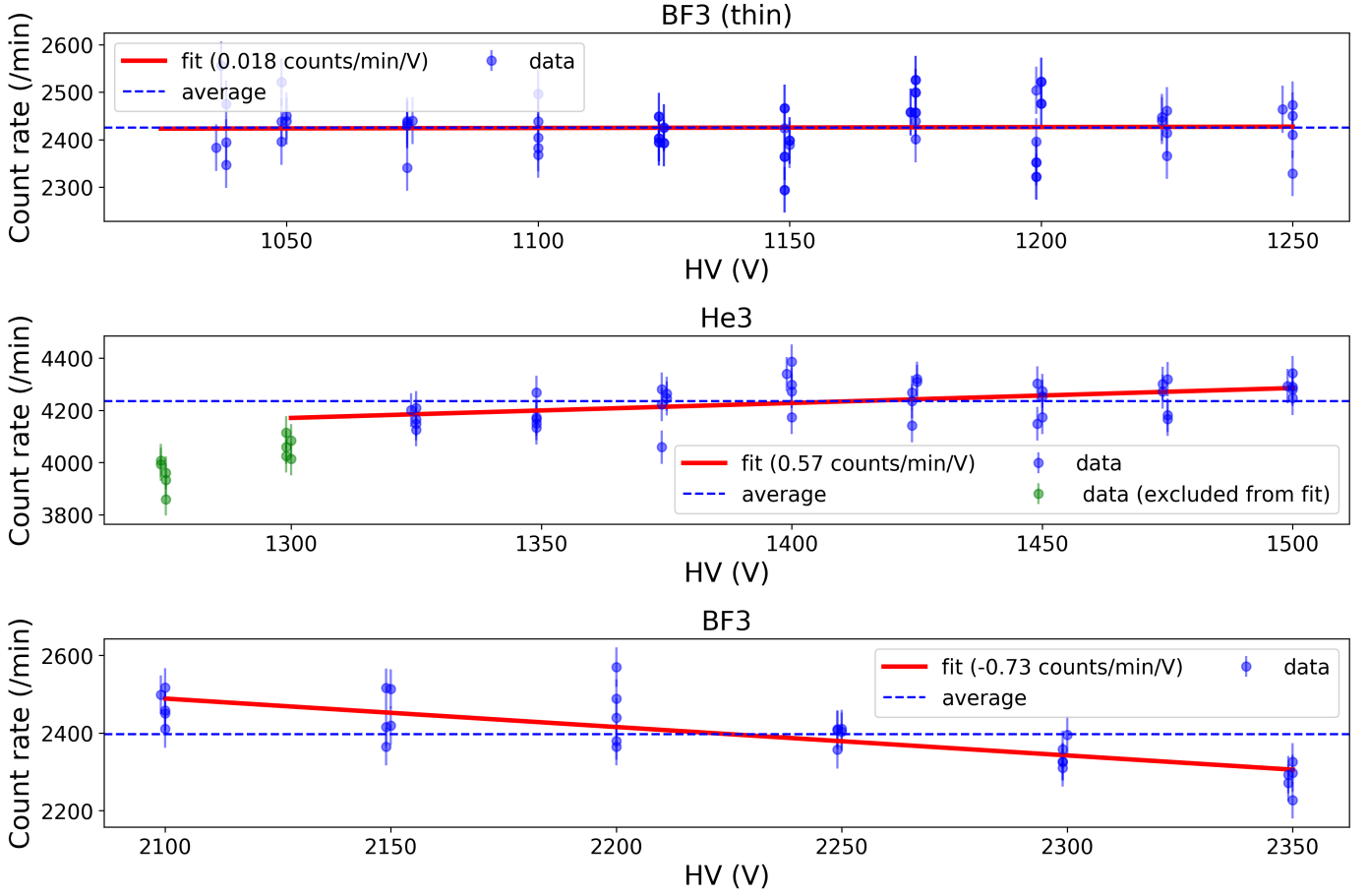


Fig. 6: The dependence of the observed count rate on variations of the HV, as measured for different tubes. The average count rate for each tube is indicated by the dashed line, while the red line shows the results of a linear regression. For the middle panel, green data points were excluded when performing the regression.

The results of the changing HV values are shown in Figure 6. For each tube the count rate was taken for five minutes at each voltage, and where the tests were still performed in the presence of the neutron source. The top panel shows the results for the thin BF₃ tube, and these indicate that, for this tube and in this voltage range, there is virtually no response in the count rate. A linear regression is performed (red line), resulting in a gradient of $< 0.001\%$ /V. Similar analyses for the ³He (middle panel) and thick BF₃ (bottom panel) tubes give gradients of 0.01% /V and 0.03% /V, respectively. Keeping in mind that the HV typically varies less than 1 – 3 V/min, any errors from a slowly changing HV are indeed negligible within the voltage range shown here.

4. Cosmic ray measurements: Laboratory testing

After testing with the neutron source, all three tubes were operated over December 2019 in the physics laboratory to test the pressure and temperature dependence of each tube. We also

compare the count rates of the different tubes, this time using cosmic ray neutron measurements over a time interval where the cosmic ray levels were approximately constant. The tests were done in Potchefstroom, South Africa, at a cutoff rigidity of $P_c \sim 7.2$ GV (26° 43' S, 27° 06' E, 1335 m.a.s.l.).

4.1. Pressure correction

The primary correction that needs to be performed on the count rate is a pressure correction due to the changing atmospheric depth above the monitor. The measured count rate, N , changes according to the following relation,

$$N = \langle N \rangle \exp[-\beta(P - \langle P \rangle)], \quad (5)$$

where P indicates pressure, β is the barometric coefficient of each tube, and $\langle P \rangle$ indicates the reference pressure (average over a long-time interval). Note that $-\Delta P = -(P - \langle P \rangle)$. More details can be found in e.g. Carmichael et al. (1968), Paschalis et al.

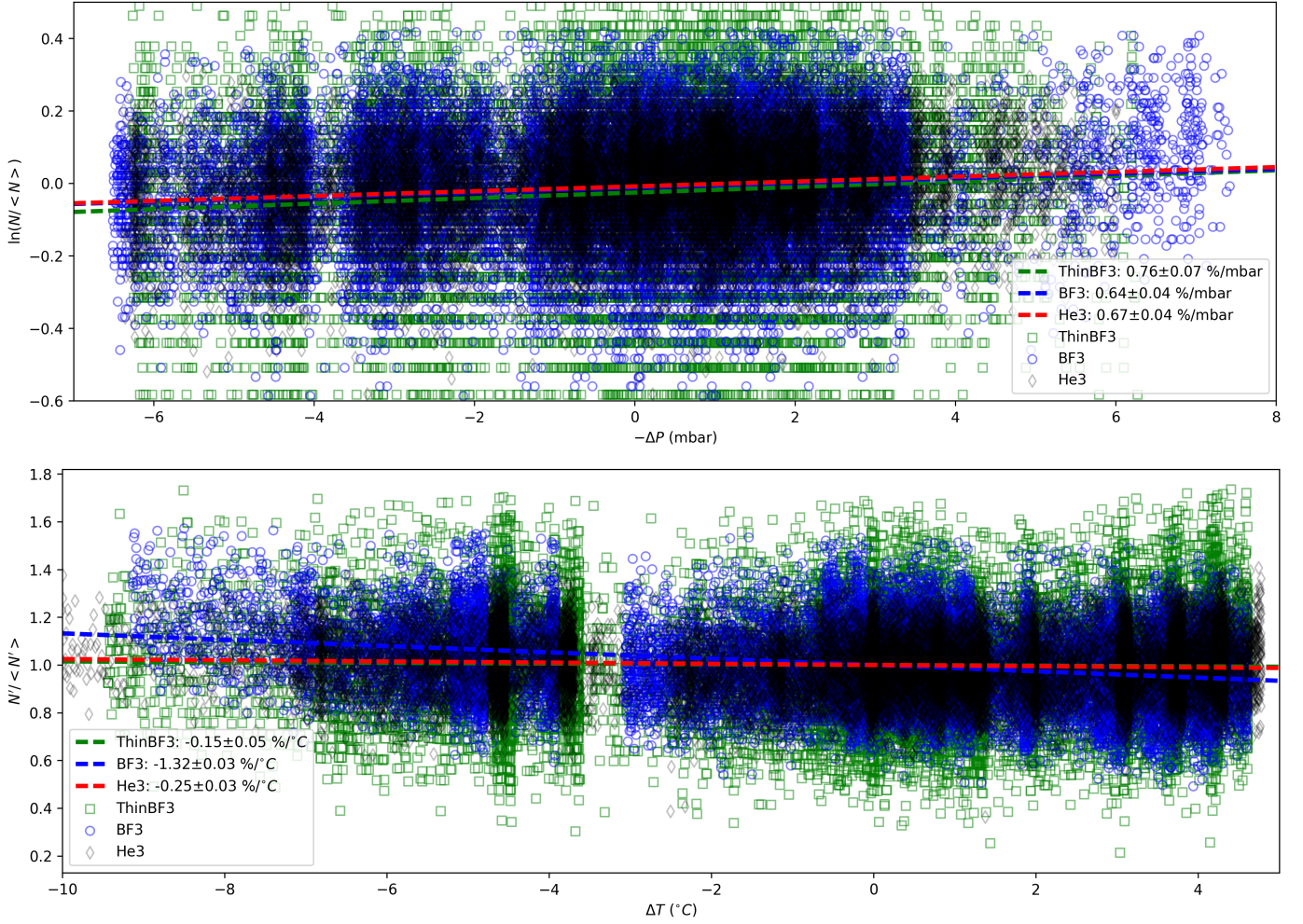


Fig. 7: The top panel shows the calculation of the barometric coefficient (the values indicated in the legend) for the different tubes (the thin BF₃ indicated by green symbols and lines, the BF₃ tube by blue, and the results for the ³He tube by red). The bottom panel is similar, but now shows a test for any temperature dependence.

(2013), Lara et al. (2016), and Bütikofer (2018).

To calculate the barometric coefficient of each tube, we plot $\ln(N/\langle N \rangle)$ as a function of $-\Delta P$, and perform a linear regression, with the barometric coefficient being the gradient thereof. This is shown in the top panel of Figure 7 for the different tubes. The calculated barometric coefficients are indicated in the legend and are all within the range 0.65 – 0.75 %/mbar. Once these coefficients are known, we apply the pressure correction by

$$N' = N \exp(\beta \Delta P), \quad (6)$$

where N' is the pressure corrected count rate of each tube.

4.2. Temperature dependence

Previous studies (e.g. Evenson et al., 2005; Krüger et al., 2008) have shown that NM count rates are affected by temperature

variations. It should be noted that, in contrast to the real barometric effect, related to the physics of atmospheric cascade, the temperature effect is spurious and related to the stability of the detector rather than to the real changes of the neutron flux. In traditional NMs, the temperature is usually carefully maintained, and these effects are not important. However, the more mobile mini-NMs are often placed in environments with large temperature changes, and hence, we need to check for (and correct if necessary) any possible systematic temperature effects. Any temperature effects are hard to predict, and different components of the mini-NM probably react differently to temperature variations (see the discussion by Evenson et al., 2005).

The bottom panel of Figure 7 shows $N'/\langle N' \rangle$ (note this is already the pressure-corrected count rate) as a function of the temperature change $\Delta T = T - \langle T \rangle$ for the different tubes. Note that

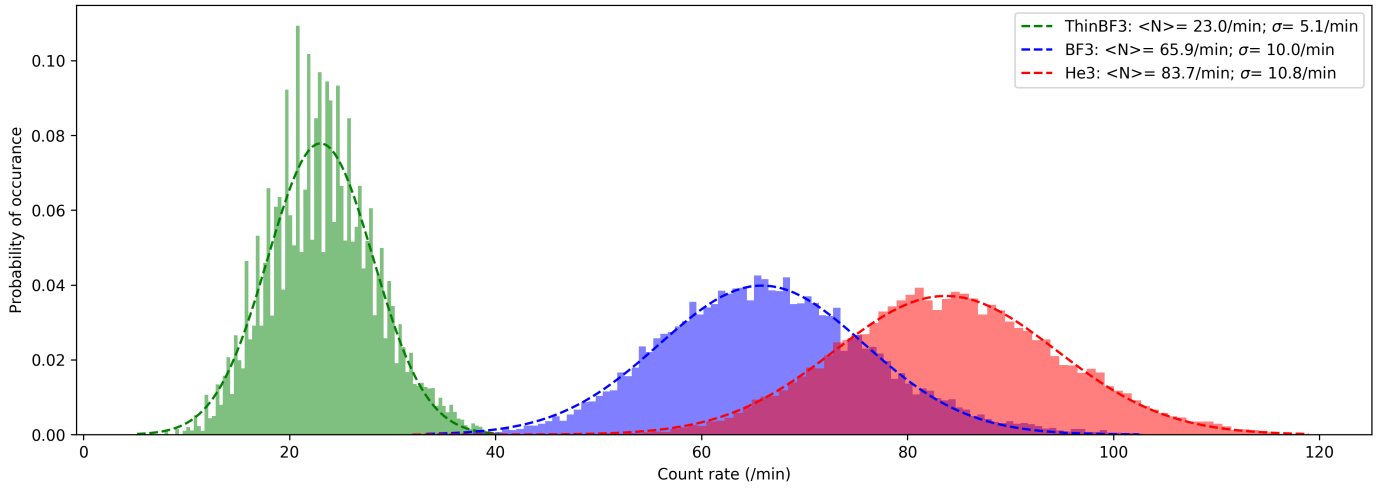


Fig. 8: Probability distribution of the count rate for each tube (histograms), fitted with a Gaussian curve (dashed lines). The legend shows the average and standard deviation of each fit.

we use the internal temperature sensor that is placed in-between the tube and the moderator. All three tubes show a negative temperature dependence, with the count rate decreasing with increasing temperature. For the thin BF_3 tube, the temperature dependence is, however, negligible, while it may become significant for the other tubes, especially if these are placed in an environment with large temperature changes. The correction for the temperature changes can be implemented as

$$N'_T = N' - \beta_T \Delta T, \quad (7)$$

where N'_T is now the temperature and pressure corrected count rate, and β_T the so-called *temperature coefficient* (i.e., the gradient of the linear regression curve). Both linear regressions discussed above go, by definition, through the origin. However, depending on the mini-NM set-up and its dependence on the local environmental conditions, a linear regression may not be sufficient, and higher-order polynomials might be required. Some earlier works have also implemented exponential functions (e.g., Heber et al., 2015), which can be reduced to a linear approximation if $\beta_T \Delta T$ is sufficiently small.

Similar to the barometric coefficient, we should note that the temperature coefficient might be highly dependent on the local environmental conditions where the monitor is placed and that the pressure and/or temperature coefficients given here cannot be universally applied (see, e.g., Krüger and Moraal, 2010; Aiemsa-ad et al., 2015). Generally we do not test for any humidity or atmospheric water vapour effects (see Banglieng et al., 2020).

4.3. Comparison between the different tubes

The pressure corrected count rate from each tube is binned as a histogram, and shown in Figure 8. Gaussian distributions

are fitted to each histogram (dashed lines), showing that the remaining variations are roughly consistent with statistical cosmic ray variations. The average count rate (as derived from the fitted distribution) from each tube is indicated in the legend, along with the standard deviations. The efficiency of the different tubes are clearly illustrated in this figure: The thin BF_3 tube is, as expected, the least efficient with an average count rate of 23 counts/min, followed by the BF_3 tube with 66 counts/min, and the ^3He tube being the most efficient with a count rate of 84 counts/min. However, the increasing efficiency comes with a price, with the ^3He being, by far, the most expensive, and the thin BF_3 being, by far, the most inexpensive of the tubes tested. As such, the BF_3 tube is recommended for a standard mini-NM set-up, balancing statistical accuracy with operating costs. It should be noted that the tube used depends on the application, i.e., if one is interested in low resolution data (i.e., data or weekly averages for soil moisture measurements), then a thin BF_3 tube could still be sufficient for the task at hand.

In addition, a neutron monitor is often considered as an instrument for long-time measurements. Some cosmic ray stations have neutron monitors in operation for 50 years or even longer. In such applications, BF_3 tubes show very good stability while ^3He -filled ones can experience a long-term drift of parameters because of leakage of helium gas. On the other hand, the efficiency of BF_3 counters may also gradually decline because of deposition on the anode wire that can become notable for high-latitude, high-elevation NMs with very high count rates, such as South Pole (Bieber et al., 2007).

5. Discussion

Below we briefly describe measurements from three mini-NM stations producing long-term data, while Table 2 summarizes the current and planned mini-NM stations.

Table 2: Current and planned mini-neutron monitor stations.

| Station name | Lat. (°) | Long. (°) | Alt. (m.a.s.l.) | Tube | Comments |
|--------------------------------|--------------|---------------|-----------------|------|-------------------------|
| Current stations | | | | | |
| Dome C (Antarctica) | 75°06'S | 123°23'E | 3233 | BF3 | Lead and lead-free unit |
| Sierra Negra Peak (Mexico) | 18°59'N | 97°19'W | 4100 | BF3 | Uses older electronics |
| Riyadh (Saudi Arabia) | 24°38'N | 46°43'E | 612 | BF3 | |
| Zugspitze (Germany) | 47°25'N | 10°58'E | 2650 | BF3 | |
| Future/planned stations | | | | | |
| Addis Ababa (Ethiopia) | 9°06'N | 38°46'E | 3293 | BF3 | Deployment in 2021 |
| Chacaltaya (Bolivia) | 16°21'S | 68°07'W | 5240 | BF3 | Deployment in 2021 |
| Mobile stations | | | | | |
| SA Agulhas II (South Africa) | ~33°S – 72°S | ~ 37°W – 37°E | ~ 0 | He3 | |
| Polarstern (Germany) | ~85°N – 70°S | ~ 70°W – 20°E | ~ 0 | He3 | Uses older electronics |
| BIO Hespérides (Spain) | ~37°N – 62°S | ~ 60°W – 0°E | ~ 0 | BF3 | |

5.1. Concordia research station

A pair of mini-NMs was installed at the French-Italian research station Concordia (Dome C, Antarctic plateau) at 75°06' S, 123°23' E, 3233 m a.s.l. in 2015 (Poluianov et al., 2015; Usovkin et al., 2015). One of those instruments (called DOMC) is a standard-design unit with the lead producer and the other is “bare” (lead-free, DOMB). Both use the thick BF₃ tube discussed here. The unique location of the station (high elevation and close proximity to the geomagnetic pole) provides low atmospheric and negligible geomagnetic cutoffs. Moreover, DOMC and DOMB are ones of few NMs whose asymptotic cone point south of the equatorial plane, making it possible to study the 3D distribution of cosmic-ray variability. The average count rates of DOMC and DOMB are about 1150 and 315 counts/min, respectively, during 2019. The high altitude polar location makes these mini-NMs exceptionally sensitive to low-energy cosmic rays, which is particularly important for registration of solar energetic particles (SEPs). In confirmation of that, several SEP events have been registered since the start of the operation of mini-NMs at Concordia, including very weak ones (e.g., Mishev, Alexander et al., 2017). For example, GLE #72 on 10 September 2017 caused count rate increases of +10% (maximum 1210 cts/min with pre-increase 1102 cts/min) and +13% (maximum 330 cts/min with pre-increase 293 cts/min) at DOMC and DOMB, respectively (see the International GLE database <http://gle.oulu.fi>). Introduction of those instruments to the neutron monitor global network significantly increased its overall sensitivity to SEPs and led to a revision of the ground level enhancement (GLE) definition with the introduction of the sub-GLE class of events (Poluianov et al., 2017). In 2019, neutron monitors DOMC and DOMB were upgraded with the electronics described in this paper (in November and August, respectively). Before that, their electronics were similar to one in Krüger and Moraal (2013).

5.2. Neumayer III

A mini-NM (using a thick BF₃ tube) was installed at the German Antarctic Neumayer III research station early in 2011 (Heber et al., 2015). Neumayer III is located on the Ekström Ice-shelf

in the Atka-bay in the Weddell-sea at 70° 40 S, 8°16 W. The corresponding cutoff rigidity $P_c = 0.1$ GV has been calculated utilizing PLANETOCOSMICS (Desorgher et al., 2009) with the International Geomagnetic Reference Field (Finlay et al., 2010) and the Tsyganenko (1989) as model for the inner and outer Earth magnetosphere, respectively (Herbst et al., 2013). The monitor provided data from 2013 – 2017, and was primarily used to study the long-term stability of the instrument as there were few transient cosmic ray events during this period. The monitor was transport back to Kiel, Germany, in 2018, and retro-fitted with the new electronics discussed in this paper in early 2020. It is currently undergoing testing, and will be redeployed in the near future.

5.3. Polarstern

In 2011, a mini-NM with a ³He tube, was installed on the German research vessel, the Polarstern (Heber et al., 2015). The instrument has provided data since 2012, and is used to study both the long-term stability and sensitivity of the instrument, as well as the latitude effect as the ship sails each year from Germany to Antarctica.

5.4. Sierra Negra

This mini-NM was deployed on a plateau at the slope of the Sierra Negra volcano in the central part of Mexico (19.0°N, 97.3°W), where the High Altitude Water Cherenkov (HAWC) gamma ray observatory is located. The cutoff rigidity at this site is ~ 7.8 GV and the altitude is 4100 m.a.s.l., allowing relatively high count rates of ~ 840 counts/min (on January 2018). The mini-NM has been taking data since 2015, with a data gap of three months during 2016. Taking advantage of the portability of the mini-NM, an altitude survey was performed during 2014 going from the sea level up to 4580 m.a.s.l. (Lara et al., 2016). This study showed that the mini-NM is stable and performs well in the field.

6. Summary and outlook

The original purpose of the mini-NM was to develop a small and portable NM that can be used to inter-calibrate the world-wide network of NMs. These stationary monitors, placed at different altitudes and magnetic latitudes, also have different environmental conditions, and react to environmental changes differently. We believe that such an inter-calibration study could still be relevant, and should, at some point, be continued.

On the other hand, mini-NMs stations have produced valuable data and scientific insights, especially at polar regions and high altitudes where the mini-NM count rates are comparable to full-scale sea-level NMs. We firmly believe that this trend will continue, and, in the future, a world-wide network of mini-NMs will co-exist with the current network of NMs, especially covering current observational gaps (e.g., the sparse coverage over the Southern Hemisphere including African and South America). The mini-NMs are much more cost-effective to construct and operate than traditional NMs, providing an intriguing possibility to also retrofit older stations that were decommissioned in the past due to financial constraints with low maintenance mini-NMs. Most of these sites already have the necessary infrastructure (including power and, in some cases, internet access). Potential sites include Sulphur Mountain, Canada, at 2383 m, the site of the original NM64 monitor.

Acknowledgements. Operation of DOMC/DOMB mini-NMs is supported by projects CRIPA and CRIPA-X (No. 304435) of the Academy of Finland, Finnish Antarctic Research Program (FINNARP). DOMC/B NM data can be obtained from <http://cosmicrays.oulu.fi>, courtesy of the Sodankylä Geophysical Observatory. Operation of DOMB/DOMB NMs are possible thanks to the hospitality of the Italian polar programme PNRA (via the LTCPPA PNRA 2015/AC3 project) and the French polar Institute IPEV. The neutron monitor database NMDB (<http://nmdb.eu>) founded under the European Union's FP7 programme (contract no. 213007) is acknowledged for hosting and providing data. We acknowledge support from the MINECO - FPI 2017 program, co-financed by the European Social Fund. This work has been supported by the project CTM2016-77325-C2-1-P, funded by Ministerio de Economía y Competitividad, and by the European Regional Development Fund, FEDER. This work is based on the research supported in part by the National Research Foundation of South Africa (NRF grant number: 119424). Opinions expressed and conclusions arrived at are those of the authors and are not necessarily to be attributed to the NRF. Figures prepared with Matplotlib ([Hunter, 2007](#)).

References

- Aiemsad, N., D. Ruffolo, A. Sáiz, P. S. Mangeard, T. Nutaro, et al., 2015. Measurement and simulation of neutron monitor count rate dependence on surrounding structure. *Journal of Geophysical Research (Space Physics)*, **120**(7), 5253–5265. 10.1002/2015JA021249. [4.2](#)
- Banglieng, C., H. Janthaloet, D. Ruffolo, A. Sáiz, W. Mitthumsiri, et al., 2020. Tracking Cosmic-Ray Spectral Variation during 2007 - 2018 Using Neutron Monitor Time-delay Measurements. *Astrophys. J.*, **890**(1), 21. 10.3847/1538-4357/ab6661. [4.2](#)
- Bieber, J. W., J. M. Clem, D. Desilets, P. Evenson, D. Lal, C. Lopate, and R. Pyle, 2007. Long-term decline of South Pole neutron rates. *Journal of Geophysical Research (Space Physics)*, **112**(A12), A12102. 10.1029/2006JA011894. [4.3](#)
- Bieber, J. W., J. M. Clem, M. L. Duldig, P. A. Evenson, J. E. Humble, and R. Pyle, 2004. Latitude survey observations of neutron monitor multiplicity. *Journal of Geophysical Research (Space Physics)*, **109**(A12), A12106. 10.1029/2004JA010493. [3.2](#)
- Bütikofer, R. Ground-Based Measurements of Energetic Particles by Neutron Monitors, 95–111. Springer International Publishing, 2018. ISBN 978-3-319-60051-2. [1](#), [4.1](#)
- Caballero-Lopez, R. A., 2016. An estimation of the yield and response functions for the mini neutron monitor. *Journal of Geophysical Research (Space Physics)*, **121**(8), 7461–7469. 10.1002/2016JA022690. [1](#)
- Carmichael, H., M. Bercovitch, M. A. Shea, M. Magidin, and R. W. Peterson, 1968. Attenuation of neutron monitor radiation in the atmosphere. *Canadian Journal of Physics Supplement*, **46**, 1006. 10.1139/p68-405. [4.1](#)
- Clem, J. M., and L. I. Dorman, 2000. Neutron Monitor Response Functions. *Space Sci. Rev.*, **93**, 335–359. 10.1023/A:1026508915269. [1](#)
- Desorgher, L., K. Kudela, E. Flückiger, R. Bütikofer, M. Storini, and V. Kalgae, 2009. Comparison of Earth's magnetospheric magnetic field models in the context of cosmic ray physics. *Acta Geophysica*, **57**(1), 75–87. 10.2478/s11600-008-0065-3. [5.2](#)
- Dyer, C., A. Hands, F. Lei, P. Truscott, K. A. Ryden, P. Morris, I. Getley, L. Bennett, B. Bennett, and B. Lewis, 2009. Advances in Measuring and Modeling the Atmospheric Radiation Environment. *IEEE Transactions on Nuclear Science*, **56**(6), 3415–3422. [1](#)
- Dyer, C., F. Lei, A. Hands, and P. Truscott, 2007. Solar Particle Events in the QinetiQ Atmospheric Radiation Model. *IEEE Transactions on Nuclear Science*, **54**(4), 1071–1075. [1](#)
- Evenson, P., J. W. Bieber, J. Clem, and R. Pyle, 2005. Neutron Monitor Temperature Coefficients: Measurements for BF3 and 3He Counter Tubes. In Proceedings to the 29th International Cosmic Ray Conference, vol. 2 of *International Cosmic Ray Conference*, 485. [4.2](#)
- Finlay, C. C., S. Maus, C. D. Beggan, T. N. Bondar, A. Chambodut, et al., 2010. International Geomagnetic Reference Field: the eleventh generation. *Geophysical Journal International*, **183**(3), 1216–1230. 10.1111/j.1365-246X.2010.04804.x. [5.2](#)
- Heber, B., D. Galsdorf, J. Gieseler, K. Herbst, M. Walter, A. Stoessl, H. Moraal, H. Krüger, and G. Benade, 2015. Mini neutron monitor measurements at the Neumayer III station and on the German research vessel Polarstern. In 34th International Cosmic Ray Conference (ICRC2015), vol. 34 of *International Cosmic Ray Conference*, 122. [1](#), [4.2](#), [5.2](#), [5.3](#)
- Herbst, K., A. Kopp, and B. Heber, 2013. Influence of the terrestrial magnetic field geometry on the cutoff rigidity of cosmic ray particles. *Annales Geophysicae*, **31**(10), 1637–1643. 10.5194/angeo-31-1637-2013. [5.2](#)
- Hunter, J. D., 2007. Matplotlib: A 2D graphics environment. *Computing in Science & Engineering*, **9**(3), 90–95. 10.1109/MCSE.2007.55. [6](#)
- Jung, J., S. Oh, Y. Yi, P. Evenson, R. Pyle, G. Jee, J.-H. Kim, C. Lee, and J. Sohn, 2016. Installation of Neutron Monitor at the Jang Bogo Station in Antarctica. *Journal of Astronomy and Space Sciences*, **33**(4), 345–348. 10.5140/JASS.2016.33.4.345. [2](#)
- Kamal, A., ed., 2014. Particle physics. Graduate Texts in Physics, Springer. [3.3](#)
- Knoll, G. F., ed., 2010. Radiation Detection and Measurement, 4th ed. Wiley. [2](#), [3.1](#)
- Krüger, H., and H. Moraal, 2010. A calibration neutron monitor: Statistical accuracy and environmental sensitivity. *Advances in Space Research*, **46**(11), 1394–1399. 10.1016/j.asr.2010.07.008. [4.2](#)
- Krüger, H., and H. Moraal, 2013. Neutron monitor calibrations: progress report. *J. Phys.: Conf. Ser.*, **409**(1), 012,171. 10.1088/1742-

- 6596/409/1/012171". [5.1](#)
- Krüger, H., H. Moraal, J. W. Bieber, J. M. Clem, P. A. Evenson, K. R. Pyle, M. L. Duldig, and J. E. Humble, 2003. First Results of a Mobile Neutron Monitor to Intercalibrate the Worldwide Network. In Proceedings of the International Cosmic Ray Conference, vol. 6 of *International Cosmic Ray Conference*, 3441. [1](#)
- Krüger, H., H. Moraal, J. W. Bieber, J. M. Clem, P. A. Evenson, K. R. Pyle, M. L. Duldig, and J. E. Humble, 2008. A calibration neutron monitor: Energy response and instrumental temperature sensitivity. *Journal of Geophysical Research (Space Physics)*, **113**(A8), A08101. [10.1029/2008JA013229](#). [4.2](#)
- Krüger, H., H. Moraal, R. Nel, H. G. Krüger, and M. O’Kennedy, 2015. The mini neutron monitor programme. In Proceedings to the 34th International Cosmic Ray Conference, vol. 34 of *International Cosmic Ray Conference*, 223. [1](#)
- Lara, A., A. Borgazzi, and R. Caballero-Lopez, 2016. Altitude survey of the galactic cosmic ray flux with a Mini Neutron Monitor. *Advances in Space Research*, **58**(7), 1441–1451. [10.1016/j.asr.2016.06.021](#). [4.1](#), [5.4](#)
- Medina, J., J. J. Blanco, O. García, R. Gómez-Herrero, E. J. Catalán, et al., 2013. Castilla-La Mancha neutron monitor. *Nuclear Instruments and Methods in Physics Research A*, **727**, 97–103. [10.1016/j.nima.2013.06.028](#). [2](#)
- Mishev, A. L., S. A. Koldobskiy, G. A. Kovaltsov, A. Gil, and I. G. Usoskin, 2020. Updated Neutron-Monitor Yield Function: Bridging Between In Situ and Ground-Based Cosmic Ray Measurements. *Journal of Geophysical Research (Space Physics)*, **125**(2), e27433. [10.1029/2019JA027433](#). [1](#)
- Mishev, Alexander, Poluianov, Stepan, and Usoskin, Ilya, 2017. Assessment of spectral and angular characteristics of sub-GLE events using the global neutron monitor network. *SWSC*, **7**, A28. [10.1051/swsc/2017026](#), URL <https://doi.org/10.1051/swsc/2017026>. [5.1](#)
- Moraal, H., A. Benadie, D. de Villiers, J. W. Bieber, J. M. Clem, P. E. Evenson, K. R. Pyle, L. Shulman, M. L. Duldig, and J. E. Humble, 2001. A mobile neutron monitor to intercalibrate the worldwide network. In International Cosmic Ray Conference, vol. 10 of *International Cosmic Ray Conference*, 4083. [1](#)
- Paschalis, P., H. Mavromichalaki, V. Yanke, A. Belov, E. Eroshenko, M. Gerontidou, and I. Koutroumpi, 2013. Online application for the barometric coefficient calculation of the NMDB stations. *New Astron.*, **19**, 10–18. [10.1016/j.newast.2012.08.003](#). [4.1](#)
- Poluianov, S., I. Usoskin, A. Mishev, H. Moraal, H. Krüger, G. Casasanta, R. Traversi, and R. Udisti, 2015. Mini Neutron Monitors at Concordia Research Station, Central Antarctica. *Journal of Astronomy and Space Sciences*, **32**(4), 281–287. [10.5140/JASS.2015.32.4.281](#). [1](#), [5.1](#)
- Poluianov, S. V., I. G. Usoskin, A. L. Mishev, M. A. Shea, and D. F. Smart, 2017. GLE and Sub-GLE Redefinition in the Light of High-Altitude Polar Neutron Monitors. *Sol. Phys.*, **292**(11), 176. [10.1007/s11207-017-1202-4](#). [5.1](#)
- Signoretto, F., and M. Storini, 2011. A new modular cosmic-ray detector. *Astrophysics and Space Sciences Transactions*, **7**(1), 11–14. [10.5194/astra-7-11-2011](#). [2](#)
- Simpson, J. A., 2000. The Cosmic Ray Nucleonic Component: The Invention and Scientific Uses of the Neutron Monitor - (Keynote Lecture). *Space Sci. Rev.*, **93**, 11–32. [10.1023/A:1026567706183](#). [2](#)
- Taber, A., and E. Normand, 1993. Single event upset in avionics. *IEEE Transactions on Nuclear Science*, **40**(2), 120–126. [1](#)
- Tsyganenko, N. A., 1989. A magnetospheric magnetic field model with a warped tail current sheet. *Planet. Space Sci.*, **37**(1), 5–20. [10.1016/0032-0633\(89\)90066-4](#). [5.2](#)
- Usoskin, I., S. Poluianov, H. Moraal, H. Krüger, G. Casasanta, R. Traversi, and R. Udisti, 2015. A mini neutron monitor in Central Antarctica (Dome Concordia). In 34th International Cosmic Ray Conference (ICRC2015), vol. 34 of *International Cosmic Ray Conference*, 217. [1](#), [5.1](#)